

Motion-Based Motion Deblurring

Moshe Ben-Ezra and Shree K. Nayar, *Member, IEEE*

Abstract—Motion blur due to camera motion can significantly degrade the quality of an image. Since the path of the camera motion can be arbitrary, deblurring of motion blurred images is a hard problem. Previous methods to deal with this problem have included blind restoration of motion blurred images, optical correction using stabilized lenses, and special CMOS sensors that limit the exposure time in the presence of motion. In this paper, we exploit the fundamental trade off between spatial resolution and temporal resolution to construct a hybrid camera that can measure its own motion during image integration. The acquired motion information is used to compute a point spread function (PSF) that represents the path of the camera during integration. This PSF is then used to deblur the image. To verify the feasibility of hybrid imaging for motion deblurring, we have implemented a prototype hybrid camera. This prototype system was evaluated in different indoor and outdoor scenes using long exposures and complex camera motion paths. The results show that, with minimal resources, hybrid imaging outperforms previous approaches to the motion blur problem. We conclude with a brief discussion on how our ideas can be extended beyond the case of global camera motion to the case where individual objects in the scene move with different velocities.

Index Terms—Sharpening and deblurring, inverse filtering, motion, motion blur, point spread function, resolution, hybrid imaging.

1 INTRODUCTION

MOTION blur is the result of the relative motion between the camera and the scene during the integration time of the image. Motion blur can be used for aesthetic purposes, such as emphasizing the dynamic nature of a scene. It has also been used to obtain motion and scene 3D structure information [39], [7], [6], [24], [9], [41], [25], [46], [33]. Motion blur has also been used in computer graphics to create more realistic images which are pleasing to the eye [5], [31], [42], [3], [26], [10], [19]. Several representations and models for motion blur in human and machine vision have been proposed [40], [4], [12], [13].

Very often, motion blur is simply an undesired effect. It has plagued photography since its early days and is still considered to be an effect that can significantly degrade image quality. Fig. 1 shows simulated examples of images that are blurred due to simple motions of the camera. In practice, due to the large space of possible motion paths, every motion blurred image tends to be uniquely blurred. This makes the problem of motion deblurring hard.

Motion blurred images can be restored (up to lost spatial frequencies) by image deconvolution [17], provided that the motion is shift-invariant, at least locally, and that the blur function (*point spread function*, or PSF) that caused the blur is known. As the PSF is not usually known, a considerable amount of research has been dedicated to the estimation of the PSF from the image itself. This is usually done using the method of blind image deconvolution [27], [37], [18], [2], [38], [46], [8], [43], [45], [44]. PSF estimation and motion deblurring have also been addressed in image sequence processing, and in spatial super-resolution algorithms [36], [2], [20], [32], as well as in the context of temporal super-resolution [35].

Methods of blind image deconvolution generally assumes that the motion that caused the blur can be parameterized by a specific and very simple motion model, such as constant velocity motion or linear harmonic motion. Since, in practice, camera motion paths are more complex, the applicability of the above approach to real-world photography is very limited. Fig. 2 shows the result of applying matlab's blind image deconvolution to the image shown in Fig. 1b. The resulting image is clearly degraded by strong deconvolution artifacts.

Two hardware approaches to the motion blur problem, which are more general than the above methods, have been recently put forward. The first approach uses optically stabilized lenses for camera shake compensation [14], [15]. These lenses have an adaptive optical element, which is controlled by inertial sensors, that compensates for camera motion. As shown in Fig. 3, this method is effective only for relatively small exposures; images that are integrated over durations that are even as small as 1/15 of a second can exhibit noticeable motion blur due to system drift [30], [29]. The second approach uses specially designed CMOS sensors [11], [21]. These sensors prevent motion blur by selectively stopping the image integration in areas where motion is detected. It does not, however, solve the problem of motion blur due to camera shake during long exposures.

In this paper, we present a novel approach to motion deblurring of an image. Our method estimates the *continuous* PSF that caused the blur, from *sparse* real motion measurements that are taken during the integration time of the image, using energy constraints. This PSF is used to deblur the image by deconvolution.

In order to obtain the required motion information, we exploit the fundamental trade off between spatial resolution and temporal resolution by combining a high resolution imaging device (the *primary detector*) together with a simple, low cost, and low resolution imaging device (the *secondary detector*) to form a novel hybrid imaging system. While the primary detector captures an image, the secondary detector

• The authors are with the Computer Science Department, Columbia University, 1214 Amsterdam Avenue, New York, NY 10027-7003. E-mail: {moshe, nayar}@cs.columbia.edu.

Manuscript received 27 Apr. 2003; revised 18 Aug. 2003; accepted 21 Sept. 2003.

Recommended for acceptance by S. Soatto.

For information on obtaining reprints of this article, please send e-mail to: tpami@computer.org, and reference IEEECS Log Number TPAMI-0053-0403.

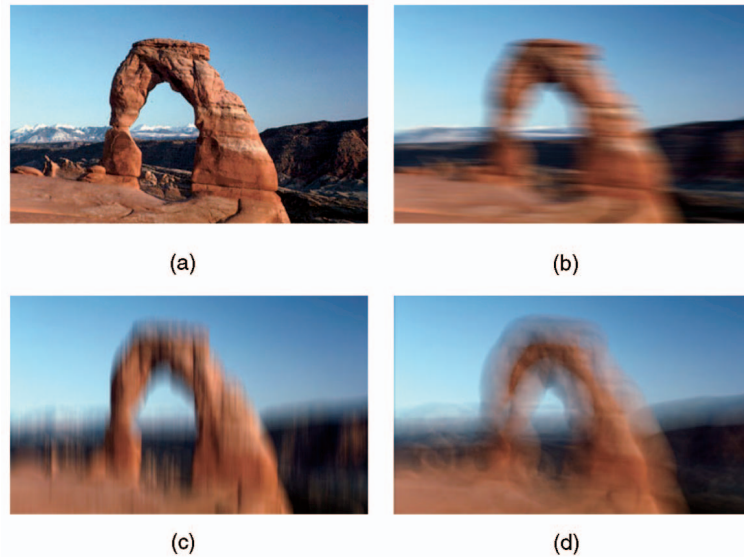


Fig. 1. Different camera motions lead to different motion blurs. Here, the unblurred scene shown in (a) is blurred using three different simulated camera rotations about the “X” and “Y” axes. These blurring functions are depth invariant and for long focal lengths also shift invariant. In (b) and (c), the scene is blurred by linear horizontal and vertical motions, respectively. In (d), the scene is blurred due to circular motion. In practice, the space of possible motion paths is very large, which makes the problem of motion deblurring without prior knowledge of the motion, very hard to solve.

obtains the required motion information for the PSF estimation.

We have conducted several simulations to verify the feasibility of hybrid imaging for motion deblurring. These simulations show that, with minimal resources, a secondary detector can provide motion (PSF) estimates with subpixel accuracy. Motivated by these results, we have implemented a prototype hybrid imaging system. We have conducted experiments with various indoor and outdoor scenes and complex motions of the camera during integration. The results show that hybrid imaging outperforms previous approaches to the motion blur problem.

Finally, we discuss the applicability of hybrid imaging to the deblurring of motion blur caused by moving objects. Moving objects present a much more complex blur problem due to their blending with the background during image integration. We show that hybrid imaging provides a partial, yet significant step towards solving this problem.

2 FUNDAMENTAL RESOLUTION TRADE OFF

An image is formed when light energy is integrated by an image detector over a time interval. Let us assume that the total light energy received by a pixel during integration must be above a minimum level for the light to be detected. This



Fig. 2. Blind image deconvolution applied to the motion blurred image shown in Fig. 1b. The strong deconvolution artifacts are the result of incorrect PSF estimation.

minimum level is determined by the signal-to-noise characteristics of the detector. Therefore, given such a minimum level and an incident flux level, the exposure time required to ensure detection of the incident light is inversely proportional to the area of the pixel. In other words, exposure time is proportional to spatial resolution. When the detector is linear in its response, the above relationship between exposure and resolution is also linear. This is the fundamental trade off between the spatial resolution (number of pixels) and the temporal resolution (number of images per second).

This trade off is illustrated by the solid line in Fig. 4. The parameters of this line are determined by the characteristics of the materials used by the detector and the incident flux. Different points on the line represent cameras with different spatio-temporal characteristics. For instance, a conventional video camera (shown as a white dot) has a typical temporal resolution 30fps and a spatial resolution of 720×480 pixels.

Now, instead of relying on a single point on this trade off line, we could use two very different operating points on the line to *simultaneously* obtain very high spatial resolution

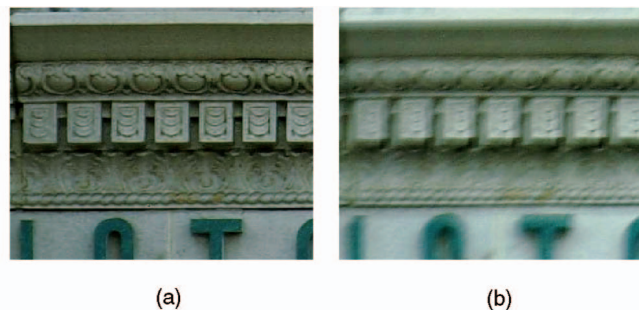


Fig. 3. The use of a stabilized lens for reducing motion blur. The image shown in (a) was taken by a hand-held camera using a 400mm stabilized Canon zoom lens at $1/250$ of a second; we can see that the stabilization mechanism works very well for this speed, producing a sharp image. In contrast, when the exposure time is raised to $1/15$ of a second, the stabilization mechanism drifts resulting in the motion blurred image shown in (b). (Printed with permission of the photographer [29]).

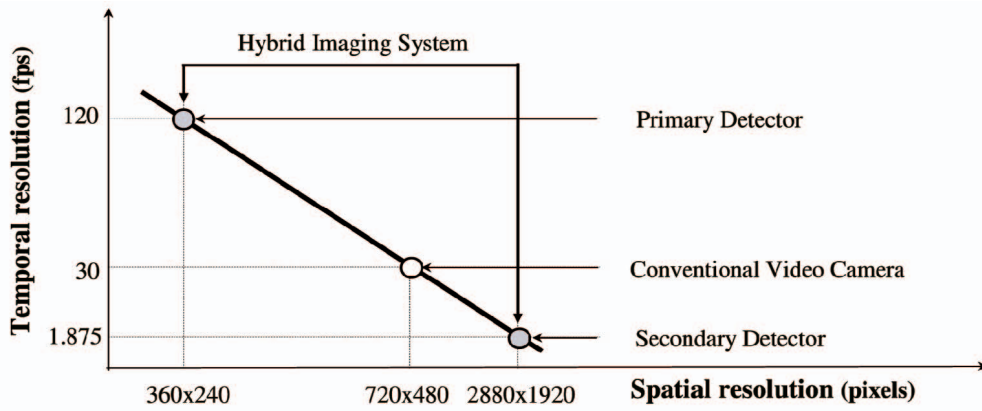


Fig. 4. The fundamental trade off between spatial resolution and temporal resolution of an imaging system. While a conventional video camera (white dot) is a single operating point on the trade off line, a hybrid imaging system uses two different operating points (gray dots) on the line, *simultaneously*. This feature enables a hybrid system to obtain the additional information needed to deblur images.

with low temporal resolution and very high temporal resolution with low spatial resolution. This type of a hybrid imaging system is illustrated by the two gray dots in Fig. 4. As we shall see, this type of hybrid imaging gives us the missing information needed to deblur images with minimal additional resources.

3 HYBRID IMAGING SYSTEMS

We now describe three conceptual designs for the hybrid imaging system. The simplest design, which is illustrated in Fig. 5a, uses a rigid rig of two cameras: a high-resolution still camera as the primary detector and a low-resolution video camera as the secondary detector. Note that this type of a hybrid camera was exploited in a different way in [34] to generate high-resolution stereo pairs using an image-based rendering approach. In our case, the secondary detector is used for obtaining motion information. Note that it is advantageous to make the secondary detector black and white since a detector collects more light energy (broader spectrum) and, therefore, can have higher temporal resolution. Also, note that the secondary detector is used only as a motion sensor; it has low resolution and high gain and is not suitable for superresolution purposes [1]. While this is a very simple design, performing the geometrical calibration between the primary and secondary detectors can be tricky since the image of the primary detector can be blurred. Moreover, the primary detector's projection model will change when the lens is replaced or the zoom setting is varied. This problem is addressed by the following two designs.

The second design uses the same lens for both detectors by splitting the image with a beam splitter. This design, which is shown in Fig. 5b, requires less calibration than the previous one since the lens is shared and, hence, the image projection models are identical. An asymmetric beam splitter that passes most of the visible light to the primary detector and reflects nonvisible wavelengths toward the secondary detector, for example a “hot mirror” [28], would be preferred.

A third conceptual design, which is illustrated in Fig. 5c, uses a special chip layout that includes the primary and the secondary detectors on the same chip. This chip has a high resolution central area (the primary detector) and a low resolution periphery (the secondary detector). Clearly, in this case, the primary and the secondary detectors would

not have the same field of view. This is possible since we assume that the motion is shift invariant. Note that such a chip can be implemented using binning technology now commonly found in CMOS (and CCD) sensors [16]. Binning allows the charge of a group of adjacent pixels to be combined before digitization. This enables the chip to switch between a normal full-resolution mode (when binning is off) and a hybrid primary-secondary detector mode (when binning is activated).

4 COMPUTING MOTION

The secondary detector provides a sequence of images (frames) that are taken at fixed intervals during the exposure time. By computing the global motion between these frames,

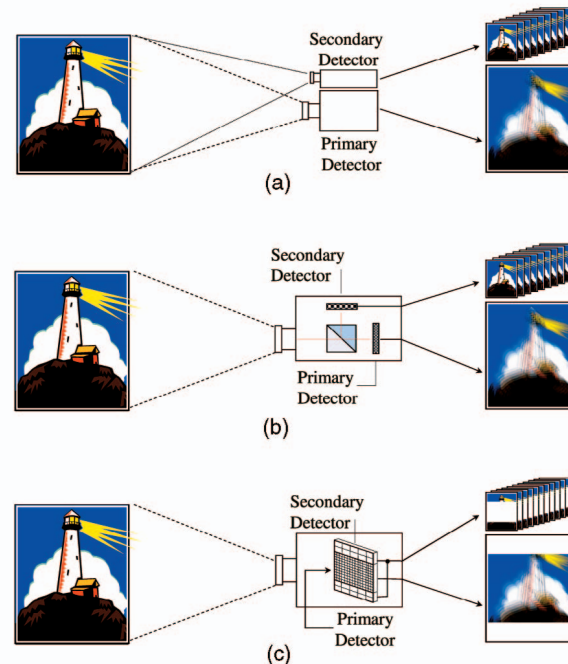


Fig. 5. Three conceptual designs of a hybrid camera. (a) The primary and secondary detectors are essentially two separate cameras. (b) The primary and secondary detectors share the same lens by using a beam splitter. (c) The primary and secondary detectors are located on the same chip with different resolutions (pixel sizes).

we obtain samples of the continuous motion path during the integration time. The motion between successive frames is limited to a global rigid transformation model. However, the path, which is the concatenation of the motions between successive frames, is not restricted and can be very complex. We compute the motion between successive frames using a multiresolution iterative algorithm that minimizes the following optical flow based error function [22]:

$$\arg \min_{(u,v)} \sum \left(u \frac{\partial I}{\partial x} + v \frac{\partial I}{\partial y} + \frac{\partial I}{\partial t} \right)^2, \quad (1)$$

where, $\frac{\partial I}{\partial x}, \frac{\partial I}{\partial y}, \frac{\partial I}{\partial t}$ are the spatial and temporal partial derivatives of the image, and (u, v) is the instantaneous motion at time t . This motion between the two frames is defined by the following global rigid motion model:

$$\begin{bmatrix} u \\ v \end{bmatrix} = \begin{bmatrix} \cos \theta & \sin \theta & \Delta x \\ -\sin \theta & \cos \theta & \Delta y \end{bmatrix} \begin{bmatrix} x \\ y \\ 1 \end{bmatrix}, \quad (2)$$

where $(\Delta x, \Delta y)$ is the translation vector and θ is the rotation angle about the optical axis.

Note that the secondary detector, which has a short but nonzero integration time, may also experience some motion blur. This motion blur can violate the constant brightness assumption, which is used in the motion computation. We assume that the computed motion between two motion blurred frames is the center of gravity of the instantaneous displacements between these frames during their integration time. We refer to this as the *motion centroid assumption*.

5 CONTINUOUS PSF ESTIMATION

The discrete motion samples that are obtained by the motion computation need to be converted into a continuous point spread function. To do that, we define the constraints that a motion blur PSF must satisfy, and then use these constraints in the PSF estimation.

Any PSF is an energy distribution function, which can be represented by a convolution kernel $k : (x, y) \mapsto e$, where (x, y) is a location and e is the energy level at that location. The kernel k must satisfy the following energy conservation constraint:

$$\iint k(x, y) dx dy = 1, \quad (3)$$

which states that energy is neither lost nor gained by the blurring operation (k is a normalized kernel). In order to define additional constraints that apply to motion blur PSFs, we use a time parameterization of the PSF with a path function $f : t \mapsto (x, y)$ and an energy function $h : t \mapsto e$. Note that the functions f and h define a curve which belongs to a subset of all possible PSFs. Due to physical speed and acceleration constraints, $f(t)$ should be continuous and at least twice differentiable. By assuming that the scene radiance does not change during image integration, we get the additional constraint:

$$\int_t^{t+\delta t} h(t) dt = \frac{\delta t}{t_{end} - t_{start}}, \delta t > 0, t_{start} \leq t \leq t_{end} - \delta t, \quad (4)$$

where $[t_{start}, t_{end}]$ is the image integration interval. This constraint states that the amount of energy which is

integrated at any time interval is proportional to the length of the interval.

Given these constraints, and the motion centroid assumption from the previous section, we can estimate a continuous motion blur PSF from the discrete motion samples, as illustrated in Fig. 6. First, we estimate the path $f(t)$ by spline interpolation as shown in Figs. 6a and 6b; spline curves are used because of their smoothness and twice differentiability properties, which satisfy the speed and acceleration constraints. In order to estimate the energy function $h(t)$ we need to find the extent of each frame along the interpolated path. This is done using the motion centroid assumption by splitting the path $f(t)$ into frames with a 1D Voronoi tessellation, as shown in Fig. 6b. Since the constant radiance assumption implies that frames with equal exposure times integrate equal amount of energy, we can compute $h(t)$ (up to scale) for each frame as shown in Fig. 6c. Note that all the rectangles in this figure have equal areas. Finally, we smooth $h(t)$ and normalize (scale) it to satisfy the energy conservation constraint. The resulting PSF is shown in Fig. 6d. The end result of the above procedure is a continuous motion blur PSF that can now be used for motion deblurring.

6 IMAGE DECONVOLUTION

Given the estimated PSF, we can deblur the high resolution image that was captured by the primary detector using existing image deconvolution algorithms [17], [23]. Since this is the only step that involves high-resolution images, it dominates the time complexity of the method, which is usually the complexity of FFT. The results reported in this paper were produced using the Richardson-Lucy iterative deconvolution algorithm [17], which is a nonlinear ratio-based method that always produces nonnegative gray-level values and, hence, gives results that make better physical sense than linear methods [17]. This method maximizes a Poisson-statistics image model likelihood function, yielding the following iteration:

$$\hat{O}^{(k+1)}(x) = \hat{O}^{(k)}(x) \cdot S(-x) \otimes \frac{I(x)}{S \otimes \hat{O}^{(k)}}, \quad (5)$$

where: I is the measured image, $\hat{O}^{(k)}$ is the k th estimation of the result, $\hat{O}^{(0)} = I$, and S is the convolution kernel (the PSF). Given that I and S are everywhere positive, $\hat{O}^{(k)}$ cannot be negative.

7 SIMULATION RESULTS

Prior to prototype implementation, two sets of simulation tests were done in order to validate the accuracy of the PSF estimation algorithm.

The first set addresses the accuracy of the motion estimation as a function of frame resolution and gray level noise. The second set illustrates the accuracy of the computed path $f(t)$ in the presence of motion blur. Both our tests were conducted using a large set of images that were synthesized from the 16 images shown in Fig. 7.

7.1 Motion Estimation Accuracy Test

In this test, we computed the motion between an image and a displaced version of the same image (representing two frames) using four different resolutions and four different levels of Gaussian noise for each resolution. The displacement

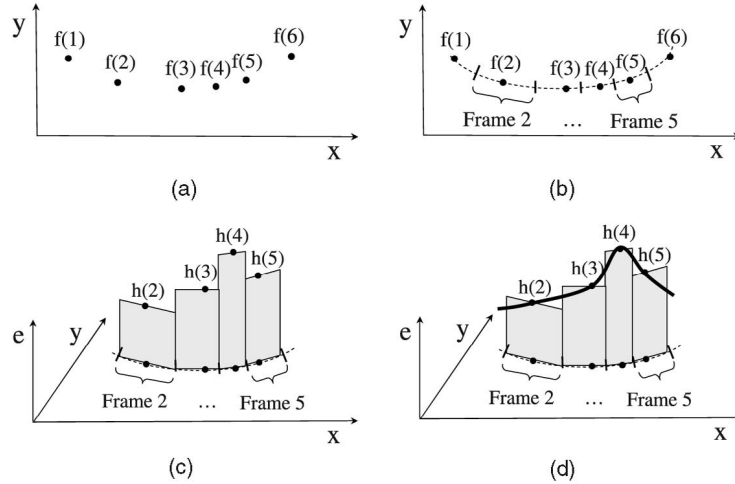


Fig. 6. The computation of the continuous PSF from the discrete motion vectors. (a) The discrete motion vectors which are samples of the function $f : t \rightarrow (x, y)$. (b) Interpolated path $f(t)$ and its division into frames by Voronoi tessellation. (c) Energy estimation for each frame. (d) The computed PSF.

used in the test was $(17, 17)$ pixels, and the noise level was varied between standard deviations of 3 to 81 gray levels. The computed displacements of the downsampled images were scaled back to the original scale and compared with the actual (ground truth) values. Table 1 shows the test results. We can see that subpixel motion accuracy was obtained for all tests except the test with the lowest image quality of 80×80 pixels and noise standard deviation of 81 gray levels. This test confirms the feasibility of using a low resolution detector to obtain accurate motion estimates.

7.2 Path Accuracy Test

Here, we first generated a dense sequence of 360 images by using small displacements of each image in the set shown in Fig. 7, along a predefined path. We then created a motion blurred sequence by averaging groups of successive frames together. Finally, we recovered the path from this sequence and compared it to the ground truth path. Table 2 shows the results computed over a set of 16 synthesized sequences, for different blur levels and different paths. We can see that subpixel accuracy was obtained for all paths. Moreover, the small standard deviation obtained for the different test sequences shows that the different textures of the test images have little effect on the accuracy of the path estimation.

8 PROTOTYPE HYBRID CAMERA RESULTS

Fig. 8 shows the prototype hybrid imaging system we have implemented. The primary detector of the system is a 3M pixel ($2,048 \times 1,536$) Nikon digital camera equipped with a $\times 6$ Kenko zoom lens. The secondary detector is a Sony DV camcorder. The original resolution of the camcorder

(720×480) was reduced to 360×240 to simulate a low resolution detector. The two sensors were calibrated using an image that was captured using a tripod (without motion blur).

Figs. 9 and 11 show results obtained from experiments conducted using the prototype system. Note that the exposure times (up to 4.0 seconds) and the focal lengths (up to 884mm) we have used in our experiments far exceed the capabilities of other approaches to the motion blur problem.

TABLE 1
Scaled Motion Estimation Error between Two Frames (in Pixels) as a Function of Resolution and Noise Level

Noise	$\sigma = 3$	$\sigma = 9$	$\sigma = 27$	$\sigma = 81$
	Error		Error	
Res.	Avg	stdv	Avg	stdv
640×640	0.01, 0.00	0.01, 0.00	0.02, 0.00	0.04, 0.00
320×320	0.03, 0.00	0.04, 0.00	0.05, 0.00	0.10, 0.01
160×160	0.03, 0.00	0.04, 0.00	0.07, 0.00	0.40, 0.14
80×80	0.13, 0.00	0.21, 0.01	0.39, 0.10	2.60, 4.49

This table shows that it is possible to obtain subpixel motion accuracy from significantly low resolution and noisy inputs.

TABLE 2
Path Estimation Error, in Pixels, as a Function of Path Type and Motion Blur

$f(t) =$	$r(\sin t, \cos t)$	$(t, \sin t)$	$(\alpha t^2, \sin t)$
	Error		Error
Blur	Avg	stdv	Avg
8 frames	0.092, 0.0000	0.099, 0.0000	0.299, 0.0001
16 frames	0.278, 0.0000	0.311, 0.0001	0.610, 0.0004

We can see that subpixel accuracy was obtained for all tests with very little deviation between different test images.



Fig. 7. The set of diverse natural images that were used in the simulation tests.

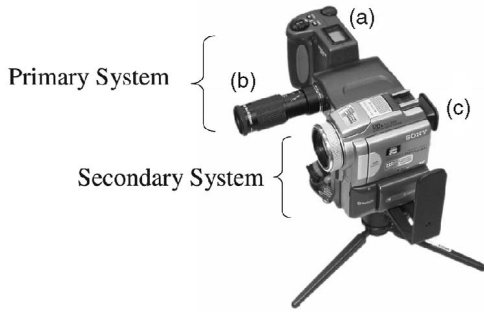


Fig. 8. The hybrid camera prototype used in the experiments is a rig of two cameras. (a) The primary system consists of a 3M pixel Nikon CoolPix camera (b) equipped with a $\times 6$ Kenko zoom lens. (c) The secondary system is a Sony DV camcorder. The Sony images were reduced in size to simulate a low-resolution camera.

In Figs. 9a, 10a, 11a, and 12a, we see the inputs for the deblurring algorithm, which includes the primary detector's blurred image and a sequence of low-resolution frames captured by the secondary detector. Figs. 9b, 10b, 11b, and 12b show the computed PSFs for these images. The path shown in these figures is the camera motion, while the colors code the percentage of the total energy at each point along the path. Notice the complex motion paths and the sparse energy distributions in these PSFs. Figs. 9c, 10c, 11c, and 12c show the deblurring results. Notice the details that appear in the magnified subimages compared to the original blurred images and the ground truth images shown in Figs. 9d, 10d, and 12d, that were taken without motion blur by using a tripod. Also, notice the text on the building shown in the left column of Fig. 11, which is completely unreadable in the blurred image shown in Fig. 11a, and clearly readable in the deblurred image shown in Fig. 11c. Some increase of noise level and small deconvolution artifacts are observed and are expected side effects of the deconvolution algorithm. Overall, however, in all the experiments the deblurred images show significant improvement in image quality and are very close to the ground truth images.

9 APPLICABILITY TO DEBLURRING OF MOVING OBJECTS

We now address the problem of motion blur due to an object moving in front of a stationary (nonblurred) background. This problem is difficult since the moving object "blends" with the background and, therefore, it is not enough to know the object's PSF to deblur the image; the blurred object must be separated from the background before it can be deblurred. This blending effect is illustrated in Fig. 13. Figs. 13a and 13b show the ground truth image and a simulated image with a blurred moving object (balloons). Fig. 13c shows the part of the image that contains the blurred foreground object. Note that the blending of the foreground and the background is clearly visible. Fig. 13d shows the result of deconvolving the foreground object with the known PSF. The resulting image has strong artifacts and does not look natural as seen in the composite image in Fig. 13e. Note that we have assumed that the extent of the blur and the shape of the mask used for compositing the deblurred foreground and the clear background are known. However, it is not obvious how these can be obtained from the blurred image in Fig. 13b without additional information.

Assuming that the blending is linear, we can express the correct deblurring operation in the presence of blending as:

$$O = (I - (B \cdot \overline{M \otimes S})) \otimes^{-1} S + B \cdot \overline{M}, \quad (6)$$

where O is the deblurred image, I is the blurred input image, S is the PSF, \otimes^{-1} denotes deconvolution, M is a segmentation mask for the shape of the foreground (nonblurred) object, B is a clear and nonblurred background image, \otimes denotes 2D convolution, and \overline{X} is the complement of X .

Note that the deblurring given by (6) requires a background image which is not only nonblurred (this is an assumption) but also void of any foreground moving object. A clear background can be obtained in several ways. One way is to capture a picture of the background when no foreground objects are present. In scenarios where foreground objects are always present, one can capture a sequence of high-resolution images which are sufficiently sparse in time, and apply a

Indoor Scene: 3D Objects (Focal length = 604mm, Exposure time = 0.5 sec.)

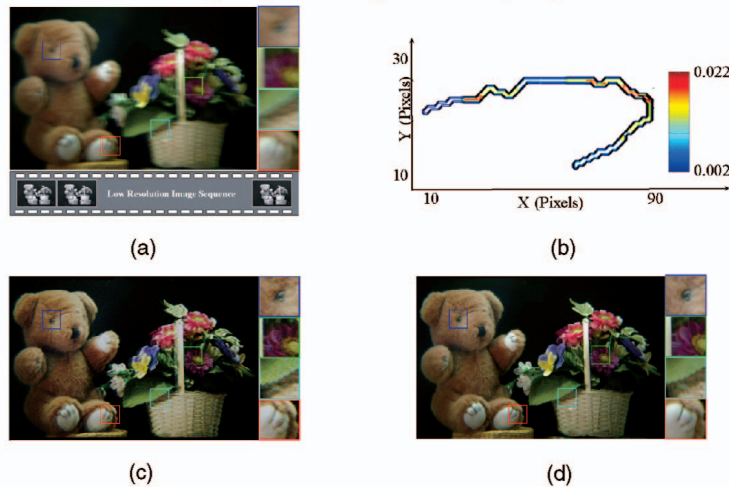


Fig. 9. Experimental results for indoor 3D objects scene. (a) Input images, including the motion blurred image from the primary detector and a sequence of low-resolution frames from the secondary detector. (b) The computed PSF. Notice the complexity of its path and its energy distribution. (c) The deblurring result. The magnified windows show details. (d) Ground truth image that was captured without motion blur using a tripod.

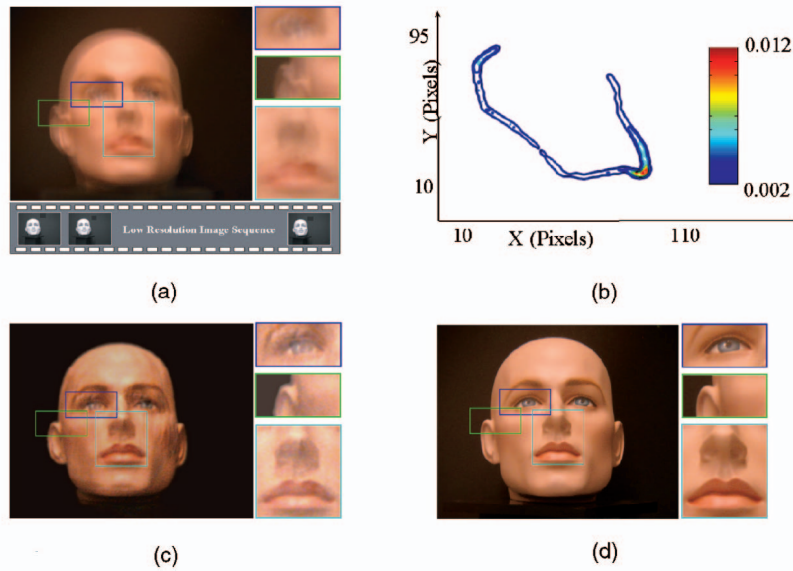
Indoor Scene: Face (Focal length = 593mm, Exposure time = 0.5 sec.)

Fig. 10. Experimental results for indoor face scene. (a) Input images, including the motion blurred image from the primary detector and a sequence of low-resolution frames from the secondary detector. (b) The computed PSF. Notice the complexity of its path and its energy distribution. (c) The deblurring result. The magnified windows show details. (d) Ground truth image that was captured without motion blur using a tripod.

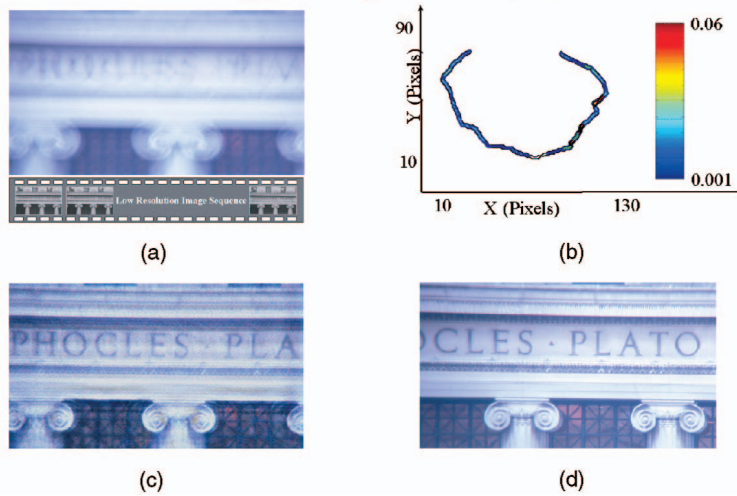
Outdoor Scene: Building (Focal length = 633mm, Exposure time = 1.0 sec.)

Fig. 11. Experimental results for outdoor building scene. (a) Input images, including the motion blurred image from the primary detector and a sequence of low-resolution frames from the secondary detector. (b) The computed PSF. Notice the complexity of its paths and its energy distribution. (c) The deblurring result. Notice the clarity of the text. (d) Ground truth image that were captured without motion blur using a tripod.

median filter to the sequence. The hybrid camera can provide an accurate PSF for the moving object; this can be done by applying a tracking algorithm to the low-resolution (high frame-rate) sequence. Since we assume shift invariance, only a single feature needs to be tracked. Hybrid imaging can also provide a low-resolution mask (shape) of the foreground object using the secondary detector's image. This is true only for the designed shown in Figs. 5a and 5b.

Fig. 14 shows how such a low-resolution mask can be effective in deblurring the image shown in Fig. 13b image using (6). Fig. 14a shows the blending mask $M \otimes S$ of the foreground. Figs. 14b and 14c show the background component $B \cdot M \otimes \bar{S}$ and the foreground component $I - (B \cdot M \otimes \bar{S})$ of the blurred image. Fig. 14d shows the deblurred foreground object and, finally, Fig. 14e shows the composite deblurred image. We can see that the low-

resolution mask was effective in avoiding any undesired blending of the foreground and the background.

The extension of this method to a blurred background scenario, where it is possible to obtain a clear nonblurred, or a clear deblurred image of the background, is straightforward. In this case, (6) becomes:

$$O = (I - ((B \otimes S_b) \cdot \overline{M \otimes S_f})) \otimes^{-1} S_f + B \cdot \bar{M}, \quad (7)$$

where S_b and S_f are the PSFs of the background and the foreground, respectively.

10 CONCLUSION

In this paper, we have presented a method for motion deblurring by using hybrid imaging. This method exploits

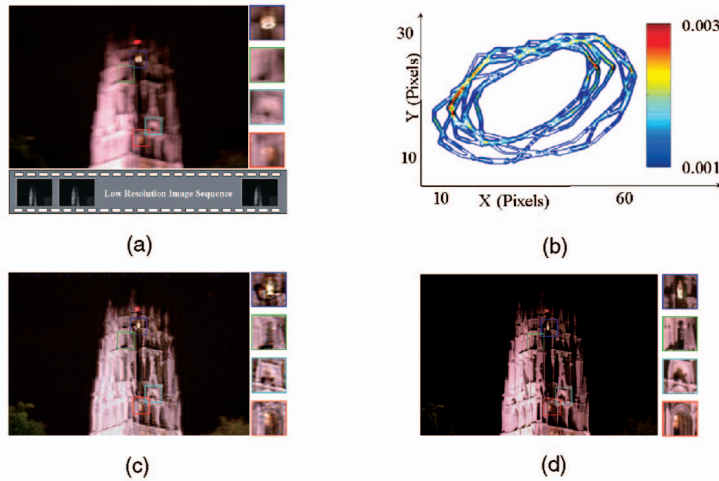
Outdoor Night Scene: Tower (Focal length = 884mm, Exposure time = 4.0 secs.)

Fig. 12. Experimental results for outdoor tower scene. (a) Input images, including the motion blurred image from the primary detector and a sequence of low-resolution frames from the secondary detector. (b) The computed PSF. Notice the complexity of its path and its energy distribution. (c) The deblurring result. (d) Ground truth image that was captured without motion blur using a tripod.

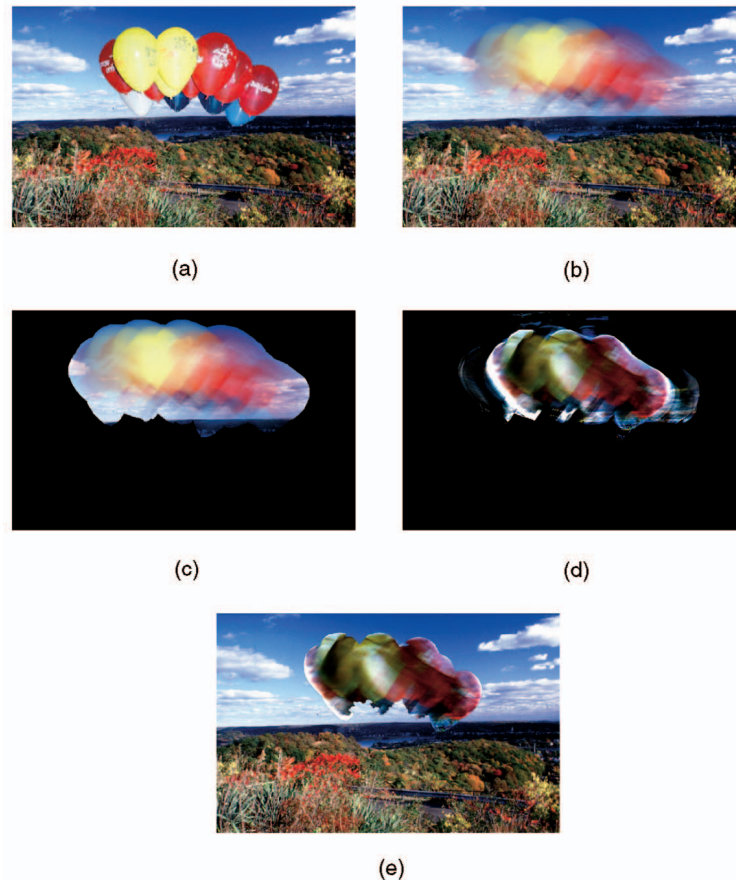


Fig. 13. Object blending problem. (a) Nonblurred ground truth image. (b) Synthetically blurred image. (c) Blurred foreground image. The nonmasked area is exactly the blur object extent. Notice that the foreground is blended with the background. (d) Deblurring of the foreground object. The artifacts due to blending are clearly visible. (e) Composite of the clear background with the deblurred foreground using a ground truth composite mask. The resulting image does not look natural.

the fundamental trade off between spatial and temporal resolution to obtain ego-motion information. We use this information to deblur the image by estimating the PSF that causes the blur. Simulation and real test results show that, with minimal resources, hybrid imaging outperforms previous approaches to the motion blur problem.

Our approach has several application. It can be applied to aerial surveillance systems where vehicle translation, which cannot be corrected by gyro-based stabilization systems, can greatly reduce the quality of acquired images. The method also provides a motion deblurring solution for consumer level digital cameras. These cameras often have small yet

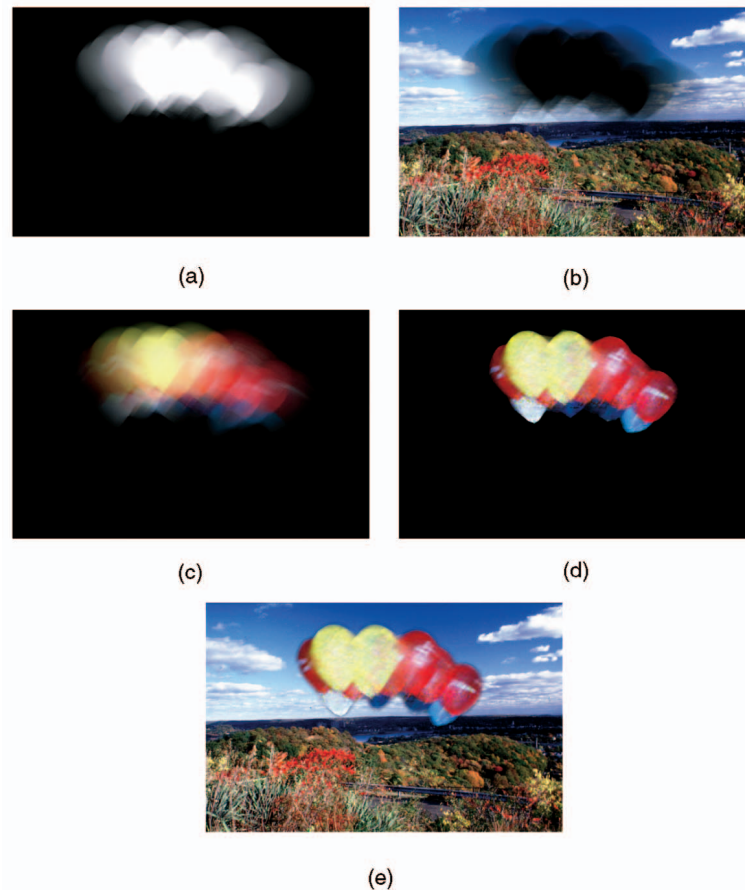


Fig. 14. Object deblurring simulation result. (a) Blending mask obtained from the secondary detector's image sequence. (b) Background component obtained from a clear background image and the blending mask. (c) Blurred foreground obtained by subtracting the background component from the primary detector's blurred image. (d) Deblurred image of the foreground object. (e) Composite of the deblurred foreground and the clear background using a low resolution mask obtained from the secondary detector.

powerful zoom lenses, which makes them prone to severe motion blur, especially in the hands of an amateur photographer. Since the method is passive, it can be implemented by incorporating a low-cost chip into the camera such as the one used in optical mice. This chip has low spatial resolution and high temporal resolution, which can be used to obtain the ego-motion information. The image deblurring process can be performed automatically, or upon user request, by the host computer that is usually used to download the images from the camera. Alternatively, the deblurring function can be incorporated into the camera itself, so that the user always sees images of the highest (motion deblurred) quality.¹ We believe that our proposed method can be applied to various domains of imaging, including, remote sensing, aerial imaging, and digital photography.

ACKNOWLEDGMENTS

This work was supported by a US National Science Foundation ITR Award (No. IIS-00-85864).

1. Note that, if the motion computation in a hybrid imaging system is done in real-time, it may be used to control an optically stabilized lens instead of the inertial sensors used today. This may enable a lens-independent optical stabilization since hybrid imaging measures the motion at the image plane and not the camera's angular motion.

REFERENCES

- [1] S. Baker and T. Kanade, "Limits on Super-Resolution and How to Break Them," *IEEE Trans. Pattern Analysis and Machine Intelligence*, vol. 24, no. 9, pp. 1167-1183, Sept. 2002.
- [2] B. Basile, A. Blake, and A. Zisserman, "Motion Deblurring and Super-Resolution from an Image Sequence," *Proc. Fourth European Conf. Computer Vision. ECCV '96*, p. 573, 1996.
- [3] G. Besuevsky and X. Pueyo, "A Motion Blur Method for Animated Radiosity Environments," *Proc. Sixth Int'l Conf. Computer Graphics and Visualization 98*, p. 35, 1998.
- [4] S. Bottini, "On the visual motion blur restoration," *Proc. Second Int'l Conf. Visual Psychophysics and Medical Imaging*, p. 143, 1981.
- [5] G.J. Brostow and I. Essa, "Image-Based Motion Blur for Stop Motion Animation," *Proc. SIGGRAPH 2001 Conf.*, p. 561, 2001.
- [6] W.-G. Chen, N. Nandhakumar, and W.N. Martin, "Image Motion Estimation from Motion Smear—A New Computational Model," *IEEE Trans. Pattern Analysis and Machine Intelligence*, vol. 18, p. 412, 1996.
- [7] P. Csillag and L. Boroczky, "Estimation of Accelerated Motion for Motion-Compensated Frame Interpolation," *Proc. SPIE Conf.*, vol. 2727, p. 604, 1996.
- [8] R. Fabian and D. Malah, "Robust Identification of Motion and Out-of-Focus Blur Parameters from Blurred and Noisy Images," *CVGIP: Graphical Models and Image Processing*, vol. 53, p. 403, 1991.
- [9] J.S. Fox, "Range from Translational Motion Blurring," *Proc. IEEE CS Conf. Computer Vision and Pattern Recognition*, p. 360, 1988.
- [10] A. Glassner, "An Open and Shut Case Computer Graphics," *IEEE Computer Graphics and Applications*, vol. 19, p. 82, 1999.
- [11] T. Hamamoto and K. Aizawa, "A Computational Image Sensor with Adaptive Pixel-Based Integration Time," *IEEE J. Solid-State Circuits*, vol. 36, p. 580, 2001.

- [12] S.T. Hammett, "Motion Blur and Motion Sharpening in the Human Visual System," *Vision Research*, vol. 37, p. 2505, 1997.
- [13] S.T. Hammett, M.A. Georgeson, and A. Gorea, "Motion Blur and Motion Sharpening: Temporal Smear and Local Contrast Non-linearity," *Vision Research*, vol. 38, p. 2099, 1998.
- [14] Canon Inc., www.canon.com/technology/optics/shakecorrect_shift/index.html, 2003.
- [15] Canon Inc., www.canon.com/technology/optics/vap/content.html, 2003.
- [16] Canon Inc., www.ropco.jp/html/tefbin.htm, 2003.
- [17] P.A. Jansson, *Deconvolution of Image and Spectra*, second ed. Academic Press, 1997.
- [18] Y. Jianchao, "Motion Blur Identification Based on Phase Change Experienced After Trial Restorations," *Proc. Sixth Int'l Conf. Image Processing (ICIP '99)*, p. 180, 1999.
- [19] C. Kolb, D. Mitchell, and P. Hanrahan, "A Realistic Camera Model for Computer Graphics," *Computer Graphics*, vol. 29, pp. 317-324, 1995.
- [20] S.H. Lee, N.S. Moon, and C.W. Lee, "Recovery of Blurred Video Signals Using Iterative Image Restoration Combined with Motion Estimation," *Proc. Int'l Conf. Image Processing*, p. 755, 1997.
- [21] X. Liu and A. El Gamal, "Simultaneous Image Formation and Motion Blur Restoration via Multiple Capture," *Proc. 2001 IEEE Int'l Conf. Acoustics, Speech, and Signal Processing*, p. 1841, 2001.
- [22] B.D. Lucas and T. Kanade, "An Iterative Image Registration Technique with Anapplication to Stereo Vision," *Defense Advanced Research Projects Agency, DARPA81*, pp. 121-130, 1981.
- [23] D.P. MacAdam, "Digital Image Restoration by Constrained Deconvolution," *J. Optical Soc. of Am.*, vol. 60, no. 12, pp. 1617-1627, Dec. 1970.
- [24] D. Majchrzak, S. Sarkar, B. Sheppard, and R. Murphy, "Motion Detection from Temporally Integrated Images," *Proc. 15th Int'l Conf. Pattern Recognition*, p. 836, 2000.
- [25] S.S. Makkad and J.S. Fox, "Range from Motion Blur," *Optical Eng.*, vol. 32, p. 1915, 1993.
- [26] N.L. Max and D.M. Lerner, "A Two-and-a-Half-D Motion-Blur Algorithm," *Computer Graphics*, vol. 19, p. 85, 1985.
- [27] C. Mayntx, T. Aach, and D. Kunz, "Blur Identification Using a Spectral Inertia Tensor and Spectral Zeros," *Proc. Sixth Int'l Conf. Image Processing (ICIP '99)*, p. 885, 1999.
- [28] Edmund Industrial Optics, www.edmundoptics.com/iod/displayproduct.cfm?productid=1492, 2003.
- [29] Digital Photo Outback, www.outbackphoto.com/reviews/equipment/canon_is_100_400/canon_is_100_400.html, 2000.
- [30] Popular Photography, www.popularphotography.com/camera/articledisplay.asp?articleid=59, 2000.
- [31] M. Potmesil and I. Chakraborty, "Modeling Motion Blur in Computer-Generated Images," *Computer Graphics*, vol. 17, p. 389, 1983.
- [32] A. Rav-Acha and S. Peleg, "Restoration of Multiple Images with Motion Blur in Different Directions," *Proc. Fifth IEEE Workshop Applications of Computer Vision (WACV 2000)*, p. 22, 2000.
- [33] I.M. Rekleitis, "Optical Flow Recognition from the Power Spectrum of a Single Blurred Image," *Proc. Third IEEE Int'l Conf. Image Processing*, p. 791, 1996.
- [34] H.S. Sawhney, Y. Guo, K. Hanna, R. Kumar, S. Adkins, and S. Zhou, "Hybrid Stereo Camera: An IBR Approach for Synthesis of Very High Resolution Stereoscopic Image Sequences," *Proc. SIGGRAPH 2001 Conf.*, p. 451, 2001.
- [35] E. Shechtman, Y. Caspi, and M. Irani, "Increasing Space-Time Resolution in Video," *Proc. Seventh European Conf. Computer Vision*, vol. 1, p. 753, 2002.
- [36] H. Shekarforoush and R. Chellappa, "Data-Driven Multi-Channel Super-Resolution with Application to Video Sequences," *J. Optical Soc. of Am. A*, vol. 16, no. 3, pp. 481-492, 1999.
- [37] A. Stern and N.S. Kopeika, "Analytical Method to Calculate Optical Transfer Functions for Image Motion and Vibrations Using Moments," *J. Optical Soc. of Am. A (Optics, Image Science and Vision)*, vol. 14, p. 388, 1997.
- [38] A. Stern, I. Kruchakov, E. Yoavi, and N.S. Kopeika, "Recognition of Motion-Blurred Images by Use of the Method of Moments," *Applied Optics*, vol. 41, p. 2164, 2002.
- [39] D.L. Tull and A.K. Katsaggelos, "Regularized Blur-Assisted Displacement Field Estimation," *Proc. Third IEEE Int'l Conf. Image Processing*, p. 85, 1996.
- [40] J.Y.A. Wang and E.H. Adelson, "Representing Moving Images with Layers," *IEEE Trans. Image Processing*, vol. 3, no. 5, pp. 625-638, Sept. 1994.
- [41] Y.F. Wang and P. Liang, "3D Shape and Motion Analysis from Image Blur and Smear: A Unified Approach," *Proc. IEEE Sixth Int'l Conf. Computer Vision*, p. 1029, 1998.
- [42] M.M. Wloka and R.C. Zeleznik, "Interactive Real-Time Motion Blur," *Visual Computer*, vol. 12, p. 283, 1996.
- [43] Y. Yitzhaky, G. Boshusha, Y. Levy, and N.S. Kopeika, "Restoration of an Image Degraded by Vibrations Using Only a Single Frame," *Optical Eng.*, vol. 39, p. 2083, 2000.
- [44] Y. Yitzhaky and N.S. Kopeika, "Identification of the Blur Extent from Motion Blurred Images," *Proc. SPIE Conf.*, vol. 2470, p. 2, 1995.
- [45] Y. Yitzhaky, I. Mor, A. Lantzman, and N.S. Kopeika, "Direct Method for Restoration of Motion-Blurred Images," *J. Optical Soc. of Am. A (Optics, Image Science and Vision)*, vol. 15, p. 1512, 1998.
- [46] Y. Zhang, C. Wen, and Y. Zhang, "Estimation of Motion Parameters from Blurred Images," *Pattern Recognition Letters*, vol. 21, p. 425, 2000.



Moshe Ben-Ezra received the BSc, MSc, and PhD degrees in computer science from the Hebrew University of Jerusalem in 1994, 1996, and 2000, respectively. His research interests are computer vision with emphasis on real-time vision and optics. He is now at the Columbia University Vision Laboratory.



Shree K. Nayar received the PhD degree in electrical and computer engineering from the Robotics Institute at Carnegie Mellon University in 1990. He is the T.C. Chang Professor of Computer Science at Columbia University. He currently heads the Columbia Automated Vision Environment (CAVE), which is dedicated to the development of advanced computer vision systems. His research is focused on three areas: the creation of cameras that produce new forms of visual information, the modeling of the interaction of light with materials, and the design of algorithms that recognize objects from images. His work is motivated by applications in the fields of computer graphics, human-machine interfaces, and robotics. He has authored and coauthored papers that have received the Best Paper Honorable Mention Award at the 2000 CVPR Conference, the David Marr Prize at the 1995 ICCV, Siemens Outstanding Paper Award at the 1994 CVPR Conference, 1994 Annual Pattern Recognition Award from the Pattern Recognition Society, Best Industry Related Paper Award at the 1994 ICPR, and the David Marr Prize at the 1990 ICCV. He holds several US and international patents for inventions related to computer vision and robotics. He was the recipient of the David and Lucile Packard Fellowship for Science and Engineering in 1992, the National Young Investigator Award from the National Science Foundation in 1993, and the Excellence in Engineering Teaching Award from the Keck Foundation in 1995. He is a member of the IEEE.

► For more information on this or any other computing topic, please visit our Digital Library at www.computer.org/publications/dlib.